Check for updates

Cholesteric Spherical Reflectors with Tunable Color from Single-Domain Cellulose Nanocrystal Microshells

Yong Geng,* Camila Honorato-Rios, JungHyun Noh, and Jan P. F. Lagerwall*

The wavelength- and polarization-selective Bragg reflection of visible light exhibited by films produced by drying cholesteric liquid crystal (CLC) suspensions of cellulose nanocrystals (CNCs) render these biosourced nanoparticles highly potent for many optical applications. While the conventionally produced films are flat, the CLC-derived helical CNC arrangement would acquire new powerful features if given spherical curvature. Drying CNC suspension droplets does not work, because the onset of kinetic arrest in droplets of anisotropic colloids leads to severe buckling and loss of spherical shape. Here, these problems are avoided by confining the CNC suspension in a spherical microshell surrounding an incompressible oil droplet. This prevents buckling, ensures strong helix pitch compression, and produces single-domain cholesteric spherical reflector particles with distinct visible color. Interestingly, the constrained shrinkage leads to spontaneous puncturing, leaving every particle with a single hole through which the inner oil phase can be extracted for recycling. By mixing two different CNC types at varying fractions, the retroreflection color is tuned throughout the visible spectrum. The new approach adds a versatile tool in the quest to utilize bioderived CLCs, enabling spherically curved particles with the same excellent optical quality and smooth surface as previously obtained only in flat films.

1. Introduction

In today's quest to develop continuously more advanced materials yet reduce our anthropogenic footprint, a prolific research platform is provided by cellulose nanocrystals (CNCs),[1] bioderived rodlike nanoparticles made from Earth's abundant cellulose resources.[2–6] Taking inspiration from Nature's

Y. Geng, C. Honorato-Rios, J. Noh, J. P. F. Lagerwall
Department of Physics and Materials Science
University of Luxembourg
Luxembourg L-1511, Luxembourg
E-mail: yong.geng@uni.lu; jan.lagerwall@lcsoftmatter.com
C. Honorato-Rios
Sustainable and Bio-inspired Materials Department
Max Planck Institute of Colloids and Interfaces
Am Mühlenberg 1, 14476 Potsdam, Germany

The ORCID identification number(s) for the author(s) of this article can be found under https://doi.org/10.1002/adma.202305251

ingeneous use of cellulose and chitin to make materials with spectacular mechanical and optical properties,[7–9] researchers are exploring ways of harnessing CNCs to make bioderived high performance materials.[5,6,10–19] Sulfuric acid hydrolized CNCs can easily be suspended in water thanks to sulfate half ester groups providing a negative surface charge. A key quality of these suspensions is that a cholesteric liquid crystal (CLC) phase develops if the global CNC mass fraction W exceeds the stability limit of the isotropic liquid phase, $w_0 \approx 2 - 3$ wt.%. For W between w_0 and the stability limit w_1 of the cholesteric phase, where $w_1 > w_0$, the cholesteric and isotropic phases coexist.

In the cholesteric phase the CNCs spontaneously organize with long-range orientational order along the *director,* **n**, which is modulated in a helical fashion along an axis **m**⊥**n**. This helical CNC organization leads to Bragg reflection of light that is selective both in wavelength and polarization:[6,20] only the circular polarization with the same handedness as the helix (left-handed for CNC) is reflected, and only in a band $\Delta\lambda = p\Delta n$ around a central wavelength:

$$\lambda_c = \bar{n}p\cos\theta \tag{1}$$

Here p is the helix period (pitch), $\Delta n = n_\parallel - n_\perp$ is the local birefringence (with $n_\parallel$ and $n_\perp$ the refractive indices along and perpendicular to **n**, respectively), $\bar{n}$ is the average refractive index, and θ is the angle of incidence with respect to the helix axis.

If p is on the order of 0.3–0.5 μm, the retroreflected ($\theta = 0$) light is in the visible range, giving rise to what is called structural color, but equilibrium CNC suspensions have $p \approx 10$ μm and thus do not appear colored. However, if the local CNC content is raised to a threshold value $w_k \approx 5 - 15$ wt.%, the system is kinetically arrested, preserving the helical configuration during further removal of water. An arrested sessile droplet cannot shrink in the xy plane of the substrate on which it rests, hence the reduction in volume as the remaining water evaporates leads to a compression only along the substrate normal $\hat{z}$. Provided that **m** is not in the xy-plane, this anisotropic deswelling process[6,21] also compresses p, maximally so if **m** has been uniformly aligned along $\hat{z}$ prior to drying.[22]

Following this strategy, several teams produced large-scale flat CNC films with strong structural color,[23–25] recently even via

**ADVANCED
SCIENCE NEWS**

www.advancedsciencenews.com

**ADVANCED
MATERIALS**

www.advmat.de

roll-to-roll printing.[26] It would be highly desirable to translate the procedure to spherical particles, because spherical curvature gives rise to numerous fascinating and useful phenomena,[27,28] from omnidirectional selective retroreflectivity[29] to unique photonic cross communication patterns[30,31] and optical echo chamber-like internal reflections.[32] Using petroleum-based CLCs, we and other groups demonstrated that the peculiar features of spherical CLC particles, Cholesteric Spherical Reflectors (CSRs), open diverse application opportunities, in anti-counterfeiting,[31,33,34] dye and pigment replacement,[34–36] human-invisible encoding of information,[28,29,37,38] omnidirectional lasing,[39] biosensing[40,41] etc. CSRs reduce the angle dependence of the apparent color, and by mixing CSRs with red, green and blue retroreflection, *any* color can be produced by Bragg diffraction alone,[36] avoiding harmful scattering particles as well as dyes and pigments. If CSRs could be produced using CNC, this potential could be tapped using the abundantly available renewable resource that cellulose provides. Unfortunately, drying CNC suspension droplets does not work, as shown by Jativa et al.[42] and Parker et al.[43] using droplets suspended in air and in oil, respectively. Both approaches led to heavily buckled and wrinkled solid particles with p much too long for visible retroreflection.

We here solve the problem by producing and drying cholesteric CNC suspension *shells* rather than droplets. The absence of edges removes the notorious coffee ring effect and the internal oil droplet enables greatly increased pitch compression upon drying, almost to the level of flat films, while minimizing the problem with buckling and wrinkling. These advantages allow us to, for the first time, produce solid CNC microparticles with retained spherical curvature and a single-domain character with uniform radial helix orientation, giving omnidirectional visible selective retroreflection. Moreover, by mixing two CNC types at varying ratios, we can tune the color throughout the visible spectrum, as demonstrated by making cellulose CSRs with red, green as well as blue retroreflection.

2. Results and Discussion

2.1. CNC Fractionation and Microfluidic Shell Production

According to classic Onsager theory of colloidal LC formation,[44] $w_0 = 3.3ad/L$ and $w_1 = 4.5bd/L$, where d and L are the short and long extensions, respectively, of CNCs (approximated as rods to fit the theory) and a and b are conversion factors between local mass fraction w and volume fraction ϕ of CNCs, the latter impacted by the ionic strength-dependent Debye length.[25] In the phase coexistence regime, $w_0 < W < w_1$, an ideal suspension has a volume fraction of LC phase that increases linearly with W. The CNC content in the LC phase stays constant at w_1 while that of the isotropic phase remains at w_0 throughout coexistence. Because pristine CNC suspensions are strongly disperse, real suspensions are far from ideal. The most striking consequence is an extension of the coexistence range, sometimes to the point that $w_1 \approx w_k$, preventing the helix to develop uniformly throughout the sample as required for good optical properties.[3,45] To circumvent this problem, we exploit a further advantage of the CLC formation in CNC suspensions, namely that it allows efficient fractionation by CNC aspect ratio.[25,46] The details of our fractionation proce-

dure, applied to two different commercial sources of CNC (from University of Maine and Celluforce, respectively), are found in Section S1 (Supporting Information).

We flow fully liquid crystalline suspensions of the CNC fraction with greatest aspect ratio from each CNC type as middle phase in a double emulsion production of shells using a co-flow microfluidic device,[47] as shown in **Figure 1**a. As inner and outer (continuous) phases immiscible with the aqueous LC suspension we use hexadecane to which we have added 0.3 wt.% of the surfactant Span 80 to stabilize the two interfaces with the CNC suspension. We use two setups (see Experimental Section), yielding shells with outer radius r_o in the ranges 25–40 µm and 60–75 µm, respectively, and inner droplets with radius r_i about 20–30 µm and 40–60 µm, respectively. The small/large shells thus have an average thickness of 5–10/30–40 µm, see Figure 1b–f. Red dye is added to the inner phase of the large shells to better visualize shell breaking and release of the inner phase into the continuous phase.

Due to the rapid equilibration of the non-viscous fractionated CNC suspension, shells acquire very good radial helix alignment within 30 mins after production. A monodomain configuration throughout all shells is confirmed after 24 h in a closed container, preventing water loss, see Figure 1b–e. Observing the shells in transmission between crossed polarizers (c), a distinct four-fold symmetric birefringence pattern typical of radial **m** is recognized. Inserting a first-order λ plate (530 nm) into the polarizing optical microscope (POM), the shells turn orange along radii parallel to the λ-plate slow axis and blue along perpendicular radii, see Figure 1d. This proves that the CNCs orient tangentially, thus confirming the desired radial **m**.

2.2. Shell Drying

To dry shells into solid CSR particles, we open the container of the suspension, allowing water to evaporate after it has diffused through the hexadecane outer phase. This slow procedure induces significant volume shrinkage of the shells, since they are prepared with ∼97 wt.% water at the start, which leaves as a result of the drying. We monitor the process by tilting the microscope 90°, filming shells from the side as water leaves them, see Figure 1f-k, Figure S3–S4 and Movies S1–S3 (Supporting Information). The shells are asymmetric with thin top and thick bottom due to the higher density of the CNC suspension compared to hexadecane, driving the internal oil droplet to the top.

During the first 7–8 h, the shells maintain a spherical shape with shrinking r_o and the CNC alignment improves somewhat as seen by a more uniform POM texture (Figure S3, Supporting Information). Once $w = w_k$ after around 8 h, kinetic arrest sets in and smooth reorganization of CNCs is no longer possible; because they now form an arrested 3D network, further shrinkage builds up internal stress. As shown in Figure S3c-d (Supporting Information), small shells clearly deform, the thin upper part elongating upwards. The stress build-up after kinetic arrest has the same impact as the shrinkage due to polymerization of CSRs made of reactive petroleum-based mesogens around an incompressible water droplet[37]: the mechanically weakest part of the shell bulges out to accommodate the inner droplet, the volume of which is now too large to fit in the shrinking arrested CNC
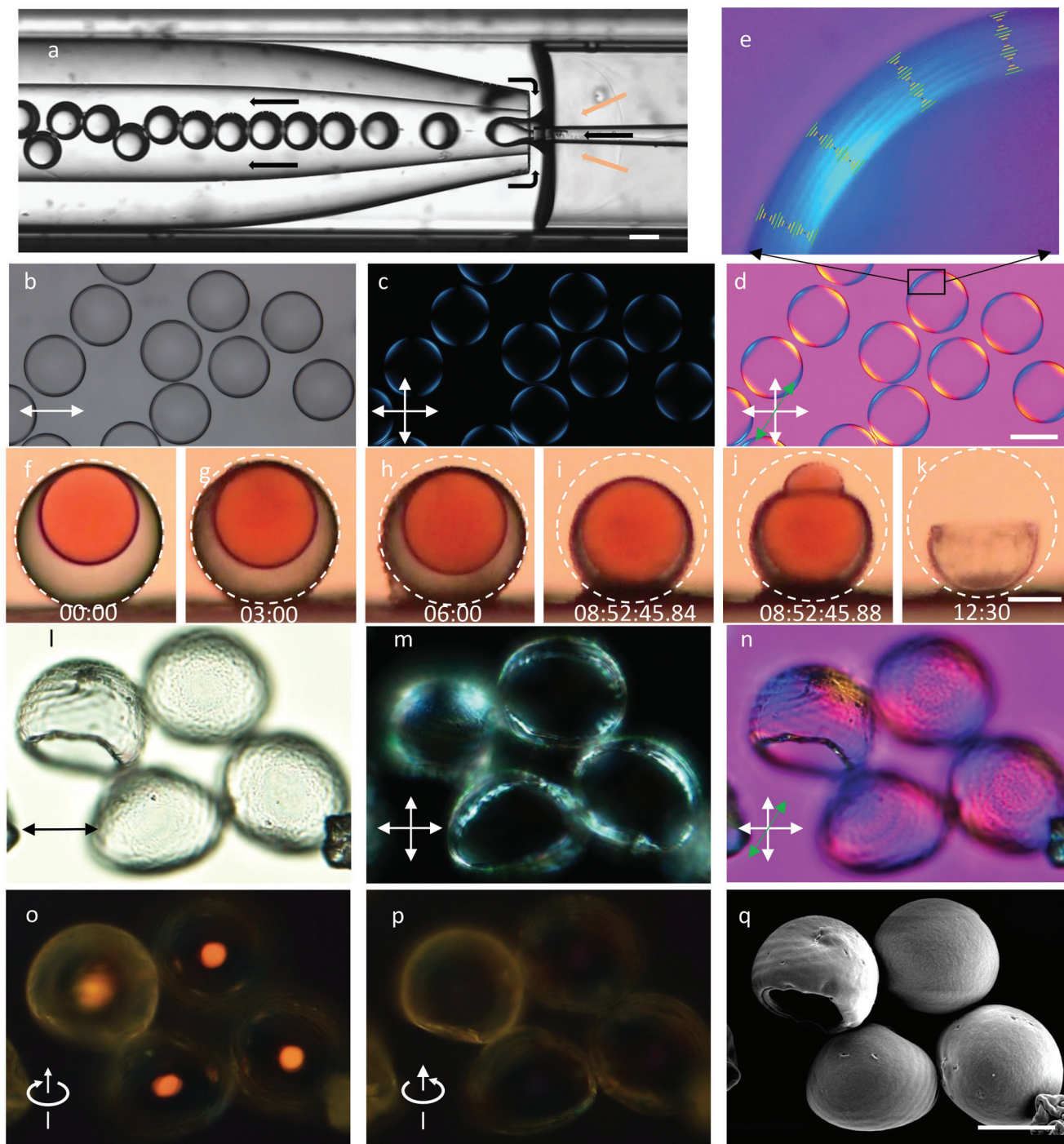
ADVANCED
SCIENCE NEWS

www.advancedsciencenews.com

ADVANCED
MATERIALS

www.advmat.de

Figure 1. a) Microscopic photo of shell production (fractionated Celluforce CNC, 2.7 wt.%) using nested glass capillary microfluidic device. Black and orange arrows indicate oil and CNC suspension flows, respectively. b –d) Shells of the same suspension with good alignment after 24 h annealing, in POM without analyzer (b), between crossed polarizers (white arrows) without (c) and with (d) λ-plate (green arrow). e) Magnification of part of one shell, revealing concentric rings that confirm the radial helix configuration; the schematic drawing indicates the helical structure. f – k) Side views (from Movie S3, Supporting Information) of a shell with dyed inner phase during drying, with time stamps on the form hh:mm and, for i–j, hh:mm:ss.ss/100; the initial outer boundary is reproduced in each panel by a white dashed circle (fractionated Celluforce CNC, 2.7 wt.%). l - q) Four dried shells (fractionated University of Maine CNC, 3.8 wt.%) viewed in transmission POM without analyzer (l), between crossed polarizers without (m) and with (n) λ-plate, and in reflection POM with left- (o) and right-handed (p) circular polarizers, respectively. Panel (q) shows the shells imaged using SEM. Scale bars are 50 µm.

suspension shell without distortion. The stress eventually gets so large that the shell ruptures, leaving a single hole bounded by a rim, as revealed by POM and SEM of the fully dried particles (Figure 1i,n,q). Following the studies of rupturing smectic LC bubbles by Stannarius and co-workers,[48] we believe the gelled CLC around the point of rupture gets temporarily fluidized by the rapid contraction, flowing down until it reaches a region that is too thick to fluidize. This process collects CNCs around the opening, creating the rim. The SEM appearance of the shells bears some resemblance to shells without a hole, where instead one part has buckled into the shell interior.[49] We confirm through a broad range of experiments, presented and discussed in the following, that the dried shells in our case indeed all have a single hole.

As seen in Figure 1f–k and Figure S4 (Supporting Information), the deformation prior to rupture appears less pronounced in the large shells (the reason is discussed in the Supporting Information), but once the hole forms the red-dyed inner phase protrudes strikingly before it diffuses into the continuous phase. As comparison, pure water shells with dyed inner oil phase were produced and the drying process was followed (Figure S5 and Movie S4, Supporting Information). Differently, water shells continuously get thinner until they break without deformation, whereafter the dyed inner phase diffuses spherically into the continuous phase.

While there is some variation in the final dried particle topology, the vast majority of dried CNC particles has the shape of a punctured sphere, see Section S3 (Supporting Information). This is highly beneficial, as the hole allows the shells to be surrounded by index matching fluid on the in- and outside to maximize optical quality,[28,37] and from a sustainability point of view it has the advantage that all oil needed to produce the CNC shells can be extracted and recycled. The geometry can be compared to that achieved by Guan et al.,[50] using polymerization-induced shrinkage as in [37], but both material and process are entirely different: rather than making shells, Guan et al. used polystyrene microparticles as solid polymerization substrates, requiring wasteful dissolution by organic solvent after polymerization, and the absence of CLC order means that their particles lack the attractive optical properties of CSRs.

Dried shells from fractionated University of Maine CNC are characterized in Figure 1l–q . Without analyzer (l), the shells are transparent with little scattering, between crossed polarizers (m) they appear grey-white where the radius is parallel neither to the polarizer nor analyzer, and with an inserted λ-plate they show the same type of color shift as in the liquid crystalline Celluforce CNC shells in (d). These textures confirm the retained radial orientation throughout the shell. Panels (o–p) show the shells in reflection POM, illuminated through and analyzed by circular polarizers. With left-hand polarizers (o) a strong red central reflection is seen, with the size depending on shell size and numerical aperture of the objective, but this is removed by switching to right-handed polarizers (p). This is the characteristic wavelength- and polarization selective omnidirectional retroreflection of CSRs. The overall smooth punctured sphere morphology is confirmed by Scanning Electron Microscopy (SEM) in (q). Lower-magnification images of many more shells from the same sample are provided in Section S4 (Supporting Information).

As reference to the shells, we dry (very slowly, see Experimental Section) sessile droplets of the highest-aspect ratio fractions of each CNC type onto a solid substrate, finding that the fractionated University of Maine CNC gives red films (Figure S1c, Supporting Information), thus with similar color to the shells. The fractionated Celluforce film is colorless, because p is too short for visible reflection (Figure S1g,h, Supporting Information). Interestingly, upon drying 1:1 and 2:1 mixtures (by mass) of fractionated University of Maine and Celluforce suspensions, we get intermediate-colored blue and green films, respectively, see **Figure 2**a,b. We now make shells following this color-tuning-by-mixing principle, obtaining blue and green retroreflection with the same mixtures, see Figure 2d,e and Section S5 (Supporting Information). In contrast to the case of drying suspended droplets, the pitch compression after gelation when drying shells is thus comparable to the situation when drying sessile droplets into flat films. This will be analyzed further below.

It is challenging to make flat CNC films uniform in color and thickness because the evaporation dynamics near a sessile droplet edge are very different from the interior.[6] This leads to the so-called 'coffee ring effect', which drives CNCs from the center to the edge, yielding thick-edged films that typically exhibit a radial color variation.[51] CNC suspension shells have no edges, hence there is no coffee ring effect during water removal, and there is no reason to expect any net flux of particles from one part of the shell to the other. This is a huge advantage in terms of obtaining uniform color in the final dried CNC particles, which exhibit clear retroreflection even at macroscopic scale, with well-defined color and high circular polarization contrast, when embedded into index matching liquid (ethyl cinnamate), as shown in Figure 2f,g. The far-field optics of CNC-based CSRs thus replicates that of petroleum-based CSRs,[28,29,34–38] rendering CNC-based CSRs suitable for generating any color.[36] The index matching liquid is the same as that in which Parker et al. suspended their crumpled CNC particles,[52] and we see that our CNC shells generate similar colors. Two differences are that the crumpled particles have larger reflection cross-section since they do not exhibit spherical symmetry, but they also lose polarization contrast at large particle size, in contrast to our shells.

The microscopic-scale appearance is shown in Figure S9 (Supporting Information). The cross communication pattern is less prominent than with petroleum-derived CSRs,[31,33,34,39–41] possibly due to the slightly modulated outside topography (see Discussion below). A solidified film with randomly distributed CNC-based CSRs still provides an unclonable and unique fingerprint, of great use in anticounterfeiting and track-and-trace applications.[28,38] All applications of CSRs can thus be achieved using biosourced CNCs, reducing the environmental footprint and extending the application targets to ingested items like foods and pharmaceuticals.

2.3. Analysis of Buckling and Pitch Compression During Drying

The difference in morphology of dried shells and dried droplets is striking when observing them next to each other, see **Figure 3**a,b: while the droplet is buckled and crumpled, the shell retains its

ADVANCED
SCIENCE NEWS

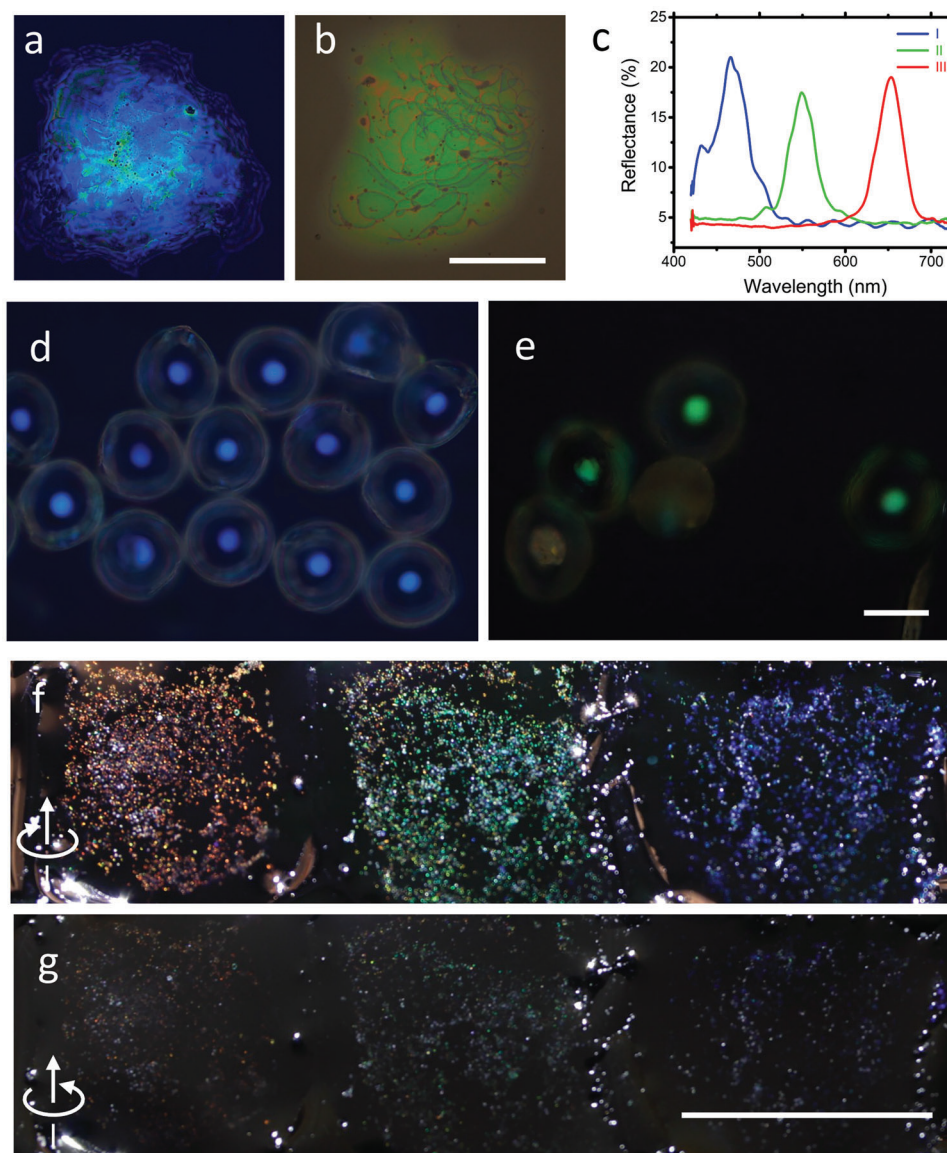www.advancedsciencenews.com

**ADVANCED
MATERIALS**

www.advmat.de

Figure 2. a,b) Left-handed circular polarization microscopy (reflection) images of films formed by slowly drying sessile droplets of mixtures of the highest aspect ratio fractions of University of Maine and Celluforce CNC, respectively, with mass ratios of 1:1 (a) and 2:1 (b). c) Reflection spectra I and II are from the films in (a) and (b), respectively, while III is from a film of pure University of Maine CNC. d,e) Left-handed circular polarization microscopy (reflection) images of dried shells produced from the same mixtures as in (a) and (b). f,g) Macroscopic images of dried large CNC shells (80–100 μm diameter) with red, green and blue retroreflection, respectively, dispersed in index matching liquid (ethyl cinnamate), taken using a regular Canon DSLR camera and white LED illumination, with left- (f) and right-handed (g) circular polariser, respectively. Scale bars in (b), (e), and (g) are 600, 50, and 5000 μm, respectively.

spherical surface intact. The physics behind the CNC shell solidification is fundamentally different from that of droplet drying, whether sessile or freely suspended, and even more different from that governing the production of petroleum-based shells, which involves photopolymerization rather than gelation driven by slow water removal, and which requires no helix compression since the precursor CLC already has p short enough for visible retroreflection. A deeper analysis is thus required to fully understand our results. We show in Section S9 (Supporting Information) and Figure 3c–e that the buckling of droplets is a consequence of the liquid crystalline order of anisotropic nanoparti-

cles in suspension, causing a mismatch in required and available spherical surface area as the droplet dries beyond kinetic arrest. Our analysis predicts that the mismatch disappears for spherical nanoparticles, congruent with observations that isotropic droplets of spherical nanoparticle suspensions can shrink without buckling.[53–55] When drying a shell of CNC suspension, the shrinkage is restrained to maintain an inner radius r_i by the inner non-volatile oil droplet, rendering the area mismatch—and thus the buckling—negligible unless the shells are very thick. This is the reason for the retained excellent spherical morphology of dried shells.
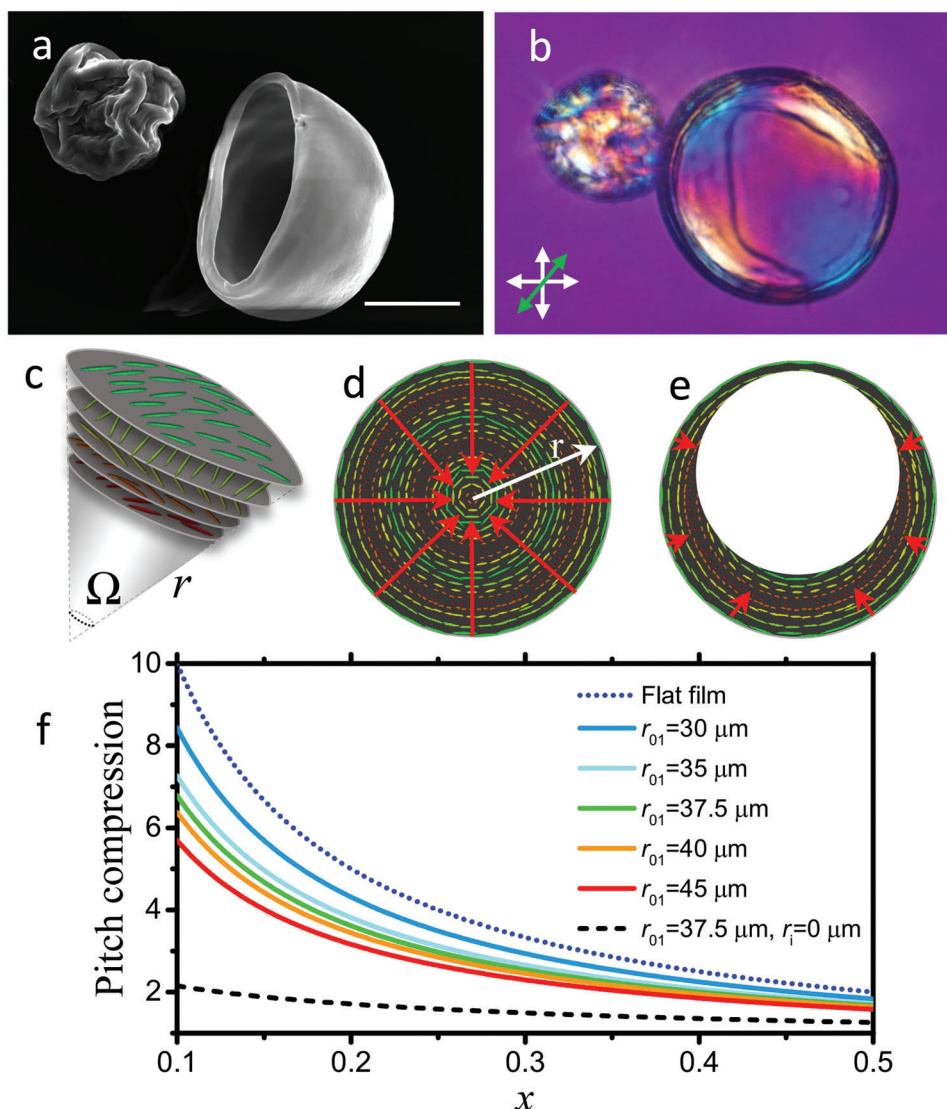
**ADVANCED
SCIENCE NEWS**

www.advancedsciencenews.com

**ADVANCED
MATERIALS**

www.advmat.de

Figure 3. a) Comparison of a droplet and a shell of CNC suspension after drying as viewed by SEM, and b) a different pair imaged by POM (scale bar—applying to both images—is 20 µm). c) Schematic illustration of the CLC arrangement of CNCs within multiple consecutive curved planes perpendicular to the radial helix, corresponding to a solid angle Ω. d,e) Illustrations of the different drying mechanisms in CNC suspension droplets (d) and shells (e); see Section S9 (Supporting Information) for details. f) The factor by which the helix pitch is compressed during shell drying as a function of the final remaining volume fraction x of the shell phase, plotted for inner droplet radius $r_i = 25$ µm (typical of our experiments) and five different initial outer radii r_{o1}; a typical value is $r_{oi} = 37.5$ µm. The black dashed line shows the dramatically lower pitch reduction for a droplet.

Apart from the buckling, dried droplets also suffer from p being too long for visible retroreflection, due to the much lower compression of the helix after kinetic arrest compared to the case of flat films with vertical helix: while the helix in an arrested sessile droplet of CNC suspension with $w_k = 10$ wt.% is compressed by a factor 10, the corresponding compression upon drying a droplet is only $10^{1/3} \approx 2.15$.[22,43] While Parker et al. later succeeded in reducing p to visible reflection ranges by post-processing,[52] the procedure further enforced the distorted wrinkled shape, hence most CSR features were lost.

The case with the shell is quite different as the incompressible inner oil droplet ensures deswelling that is much more anisotropic. Ignoring the asymmetry of the shell and the related

hole formation, we analyze the situation in Section S10 (Supporting Information), finding an effective compression factor:

$$C = \frac{r_{o1} - r_i}{[xr_{o1}^3 + (1-x)r_i^3]^{1/3} - r_i} \tag{2}$$

Here r_{o1} is the outer radius at the onset of kinetic arrest, r_i is the inner oil droplet radius, and x is the fraction of the initial volume that remains at the end of the process (thus $x = 0.1$ if $w_k = 10$ wt.%). In Figure 3f we plot equation (2) for $r_i = 25$ µm (typical of our small shells) and five different values of r_{o1} as a function of x. With the fractionated Celluforce CNCs, $w_k \approx 6.4$ wt.%. Given that some water may be left in the structure at the end of the

**ADVANCED
SCIENCE NEWS**

www.advancedsciencenews.com

**ADVANCED
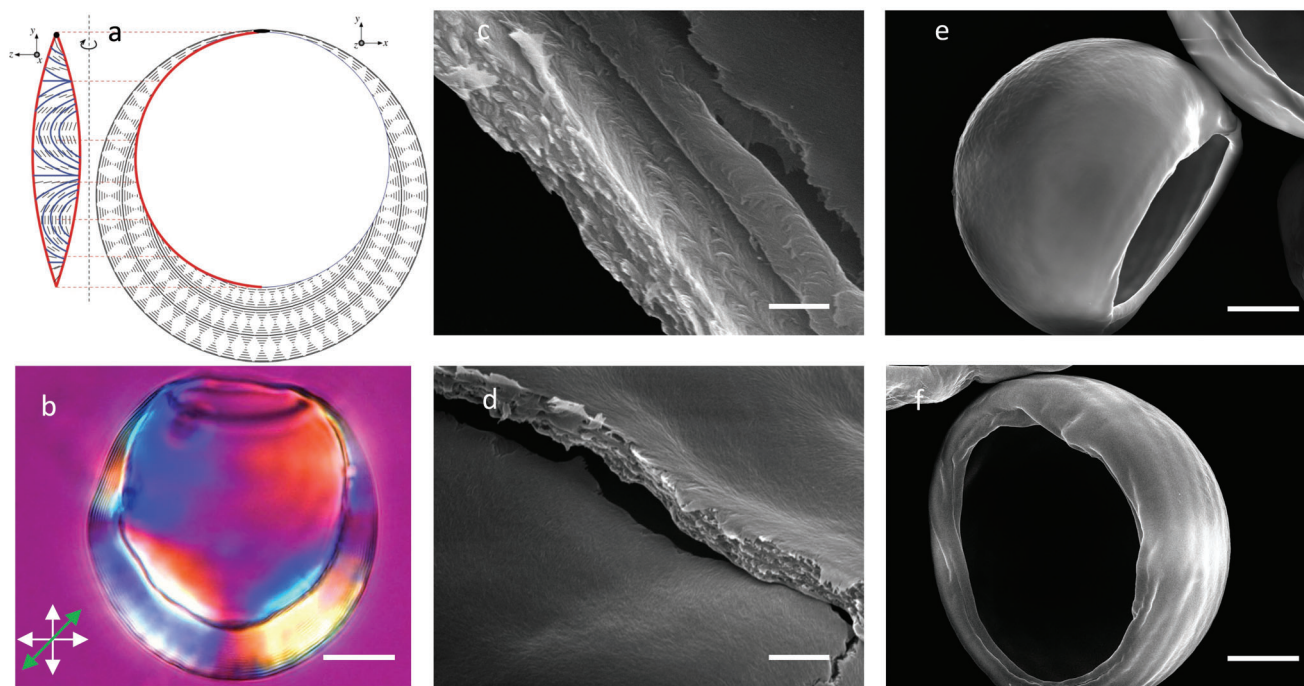MATERIALS**

www.advmat.de

Figure 4. a) Schematic illustration (redrawn from ref. [32] under CC-BY license) of the origin of the Bouligand cut arcs, here under the assumption that the cut is entirely on the inside. b) POM image obtained with first-order λ plate of a dried Celluforce CNC shell with p large enough for the helical modulation of the CNC orientation to give rise to visible periodic lines, the spacing of which is $p/2$. Note that the Bouligand cut is almost, but not entirely, on the inside. Scale bar is 50 µm. c,d) High-magnification SEM images of fractured dried Celluforce CNC shells, revealing arcs on the inside (c) but an almost smooth surface on the outside (d). Scale bars: 2 µm. e,-f) Low-magnification SEM images of shells from different perspectives, one almost smoothly spherical (e), the other somewhat wrinkled along the symmetry axis. Scale bars: 20 µm.

process, and that the density of water is lower than that of cellulose, we may as a first approximation consider $x \approx 0.1$ representative. For such a volume reduction and our typical $r_{o1} \approx 37.5$ µm, Figure 3f shows that we may expect a maximum compression of p by a factor of almost 7. This is dramatically higher than the case of CNC suspension droplets without internal oil droplet, shown for different x with the dashed black curve (which ignores the impact of buckling). The dotted blue curve, finally, shows the case of a flat film. We see that the pitch compression of thin shells can get very close to this case of maximum compression. This is a fourth major benefit of drying CNC suspensions in the form of shells rather than droplets, adding to the single opening per shell, the absence of coffee ring effect and the intact spherical shape.

2.4. Optical and Electron Microscopy Investigation of Inner and Outer Surfaces of Dried Shells

We have earlier pointed out[32] that the asymmetric character of CLC shells with thin top and thick bottom (or vice versa) by necessity creates the so-called 'Bouligand cut' structure,[56,57] in which periodic arcs of the director field develop along a surface that cuts a CLC obliquely with respect to **m**, see **Figure 4**a. However, the petroleum-based shells in our earlier study left no trace of **n** in SEM, hence we could not test whether primarily the in- or the outside is subject to the cut, or whether both sides are equally affected. With thick dried CNC shells, yielding a relatively long pitch due to reduced compression compared to thin shells

(see Figure 3f), the nanoparticle-derived structure leaves clear traces of the Bouligand cut in optical and electron microscopy, see Figure 4b–d.

We see in the high-magnification POM image in Figure 4b that the cut is primarily on the inside, as can be concluded by tracing the periodic dark lines in the shell, which run perpendicular to **m** wherever **n** is mainly along the viewing direction. The lines near the outer boundary extend continuously around almost the entire shell, with very few turns of the helix being cut off as the shell changes thickness. Along the inner boundary, in contrast, lines are cut-off at a rapid pace in the thinnest shell part. The fact that the Bouligand cut is primarily on the inside is also confirmed by high-magnification SEM images of the in- and outsides of fractured shells, see Figure 4c,d. On the inside (c), the characteristic arc pattern of the Bouligand cut is easy to recognize, whereas the outside (d) is almost smooth, as expected for a surface that cuts at the same height of the helix everywhere, as sketched in Figure 4a. The cross section of the shell, visualized by the fracture surface, shows the periodicity of the helix in the form of a layer-like character. While a CLC is fully continuous and has no layers, this artifact arises because the shell fractures easier when the CNCs are oriented in the fracture plane than when they are oriented perpendicular to it, leading to a periodic variation of protrusions.[6]

Figure 4e,f shows that the outside can sometimes—but not always—have a sequence of quasi-periodic rings parallel to the plane of the hole in the shell. We believe these rings are due to slight buckling after the rupture of the shell around its thinnest point, as the strained shell relaxes when the interior oil escapes

2305251 (7 of 9)

through the hole (Figure 1j,k). The resulting modulated topography may reduce the intensity of photonic cross communication, explaining the appearance of Figure S9 (Supporting Information). In Figure S11 (Supporting Information), we also show SEM images of shell cross-sections obtained by microtoming dried particles embedded in UV-cured glue.

3. Conclusions and Outlook

By fractionating CNC suspensions to extract only the highest aspect ratio CNCs, and confining fully liquid crystalline suspensions of such fractions between immiscible hexadecane oil phases, we obtain spherically shaped cholesteric liquid crystal shells that rapidly anneal with uniformly radial helix orientation. Slow removal of the water by diffusion through the oil and subsequent evaporation first shrinks the shell thickness with retained spherical shape, but once the water content is low enough for kinetic arrest to occur, the continued water removal leads to increasing internal stress, eventually rupturing the shell at its thinnest point. Because the core oil droplet minimizes radial shrinkage and maximizes helix pitch compression, thin dried shells are monodomain particles with retained excellent spherical shape and radial helix with pitch sufficiently short to generate visible retroreflection, in stark contrast to particles formed by drying CNC suspension droplets. By mixing two different CNC suspensions in varying proportions, we can tune the retroreflection color from red to blue.

Because our procedure gives access to CNC-based cholesteric spherical reflectors (CSRs) with tunable color, it opens for realizing the numerous suggested applications of CSRs, from structural color-based generation of the entire visible color palette with minimum viewing angle dependence[36] to anticounterfeiting patterns[29] or markers for augmented reality and robotics,[28,38] using only renewable raw materials. In future extensions, application opportunities may transcend photonics, for instance taking advantage of the enhanced mechanical properties that a helically modulated order can give rise to. From a fundamental colloid science point of view, it will be most interesting to conduct a deeper study of mechanical compression during drying as a function of location within the asymmetric anisotropic shell, and to investigate in detail the mechanism of color tuning by mixing different CNC types. We believe that the latter is related to the different equilibrium pitch at equal concentration of the two types as well as to the different values of w_k, leading to onset of kinetic arrest with different volume fractions of water in the system and thus to different degrees of helix compression upon drying.

4. Experimental Section

CNC suspensions were purchased from CelluForce (NCV100-NAL90) and University of Maine (USA) (9004-34-6), with solid contents of about 6 and 11 wt.%, respectively. The Celluforce CNCs were never sonicated while the University of Maine CNCs were lightly sonicated during the first treatment step, following the procedure described in ref. [25]. Vials with diluted suspension were standing still for three weeks at room temperature (∼22 – 23 °C) in order to measure the cholesteric volume fraction as function of CNC content. To estimate the boundaries of the biphasic regime, a linear fit was done to the experimental data, as shown in Section S1 (Supporting Information). Pictures were taken with vials between crossed polarisers with white light illuminating from the back. The two CNC suspensions were diluted to 2.5 and 3.5 wt.%, respectively, and then fractionated via phase separation in a separatory funnel for about 2 weeks. Once the boundary between anisotropic and isotropic phases was sharp, the upper isotropic phase was removed carefully. The bottom anisotropic phases with a solid content around 2.7 and 3.8 wt.%, respectively, were collected for the shell production without further treatment.

Small shells were produced in a nested glass capillary microfluidic device, without any surface treatment. The fractionated liquid crystalline CNC suspension was flown as middle phase, with a flow rate from ∼0.003-0.01 mL min⁻¹. Hexadecane (Sigma–Aldrich) containing 0.3 wt.% of Span 80 was used as inner and continuous phase, with flow rates of ∼0.003–0.02 mL min⁻¹ and ∼0.006-0.04 mL min⁻¹, respectively. Oil Red O (Sigma–Aldrich) was sometimes added to the inner phase as red dye at 0.1 wt.% concentration. All experiments started with the oil phases only being flowed, the middle phase flow started only once the microfluidic device was fully filled with oil. This is to avoid wetting of the aqueous phase to the capillary walls. The shell production was monitored using an NX4-S3 (Integrated Design Tools, Inc.) high-speed video camera mounted on a Nikon Eclipse TS100 inverted microscope. A commercial Raydrop Double Emulsion production platform (Secoya Technology) was used for making the larger shells, at high yield. Shells dispersed in the continuous phase were collected into a Petri dish that was sealed for relaxation of the cholesteric helical structure during annealing experiments (24 h). To dry the shells, the Petri dish was opened, starting a slow process since the water must diffuse from the shells through the thick layer of oil (around 0.8 cm). The full procedure took around 5 days in an incubator (INCU-Line, VWR), with relative humidity 50–60% and temperature about 25 °C. For a faster drying process (around 48 h), a thinner oil layer (∼0.2 cm) was used. Afterward, the shells were rinsed using Hexane (Sigma–Aldrich) at least three times to remove the Hexadecane.

The optical characterization was performed with a polarizing microscope (Olympus BX51, Japan) equipped with a digital camera (Olympus DP73, Japan). The long-term monitoring of shell drying was done with a Sony Camcorder (FDR-AXP33) mounted on a Nikon microscope (Nikon ECLIPSE LV100ND) tilted by 90°. Reflection spectra were obtained using an Avantes AvaSpec-2048 spectrophotometer using left-handed polarized white illumination. A microtome (Leica RM2200) was used to slice shells with 20μm steps after it had been embedded in UV-cured glue (Norland Optical Adhesive 160) for support. SEM imaging was done using a JEOL JSM-6010LA (Akishima, Japan), operated in 15–20 kV range using an In-lens secondary electron detector. For SEM imaging, samples were gold coated (around 5 nm thickness) using a Quorum Q150R ES coater (Quorum Technologies Ltd, Laughton, East Sussex, England).

Supporting Information

Supporting Information is available from the Wiley Online Library or from the author.

Conflict of Interest

The authors declare no conflict of interest.

Data Availability Statement

All raw data for this article is openly available at https://osf.io/v2kh5/.

Keywords

[1] J.-F. Revol, L. Godbout, D. Gray, *J. Pulp Pap. Sci.* **1998**, *24*, 146.
[2] D. Klemm, F. Kramer, S. Moritz, T. Lindstrom, M. Ankerfors, D. Gray, A. Dorris, *Angew. Chem., Int. Ed.* **2011**, *50*, 5438.
[3] J. P. F. Lagerwall, C. Schütz, M. Salajkova, J. Noh, J. H. Park, G. Scalia, L. Bergström, *NPG Asia Mater.* **2014**, *6*, 80.
[4] E. Kontturi, P. Laaksonen, M. Linder, Nonappa, A. Gröschel, O. Rojas, O. Ikkala, *Adv. Mater.* **2018**, *30*, 1703779.
[5] D. G. Gray, *Carbohydr. Polym.* **2020**, *250*, 116888.
[6] C. Schütz, J. R. Bruckner, C. Honorato-Rios, Z. Tosheva, M. Anyfantakis, J. P. Lagerwall, *Crystals* **2020**, *10*, 199.
[7] J. C. Weaver, G. W. Milliron, A. Miserez, K. Evans-Lutterodt, S. Herrera, I. Gallana, W. J. Mershon, B. Swanson, P. Zavattieri, E. DiMasi, D. Kisailus, *Science* **2012**, *336*, 1275.
[8] M. Mitov, *Soft Matter* **2017**, *13*, 4176.
[9] A. Almeida, J. Canejo, S. Fernandes, C. Echeverria, P. Almeida, M. Godinho, *Adv. Mater.* **2018**, *30*, 1703655.
[10] D. G. Gray, *Nanomaterials* **2016**, *6*, 213.
[11] S. N. Fernandes, P. L. Almeida, N. Monge, L. E. Aguirre, D. Reis, C. L. de Oliveira, A. M. Neto, P. Pieranski, M. H. Godinho, *Adv. Mater.* **2017**, *29*, 1603560.
[12] J. Canejo, N. Monge, C. Echeverria, S. Fernandes, M. Godinho, *Liq. Cryst. Rev.* **2017**, *5*, 86.
[13] T. P. Bigioni, X.-M. Lin, T. T. Nguyen, E. I. Corwin, T. A. Witten, H. M. Jaeger, *Nat. Mater.* **2006**, *5*, 265.
[14] R. M. Parker, G. Guidetti, C. A. Williams, T. Zhao, A. Narkevicius, S. Vignolini, B. Frka-Petesic, *Adv. Mater.* **2018**, *30*, 1704477.
[15] S. Fernandes, L. Lopes, M. Godinho, *Curr. Opin. Solid State Mater. Sci.* **2019**, *23*, 63.
[16] M. Giese, M. Spengler, *Mol. Syst. Des. Eng.* **2019**, *4*, 29.
[17] B. Frka-Petesic, S. Vignolini, *Nat. Photonics* **2019**, *13*, 365.
[18] A. Tran, C. E. Boott, M. J. MacLachlan, *Adv. Mater.* **2020**, *32*, 1905876.
[19] K. Heise, E. Kontturi, Y. Allahverdiyeva, T. Tammelin, M. B. Linder, O. Ikkala, *Adv. Mater.* **2021**, *33*, 2004349.
[20] H. De Vries, *Acta Crystallogr.* **1951**, *4*, 219.
[21] S. T. Kim, H. Finkelmann, *Macromol. Rapid Commun.* **2001**, *22*, 429.
[22] B. Frka-Petesic, G. Kamita, G. Guidetti, S. Vignolini, *Phys. Rev. Mater.* **2019**, *3*, 045601.
[23] K. Yao, Q. Meng, V. Bulone, Q. Zhou, *Adv. Mater.* **2017**, *29*, 1701323.
[24] B. Frka-Petesic, J. A. Kelly, G. Jacucci, G. Guidetti, G. Kamita, N. P. Crossette, W. Y. Hamad, M. J. MacLachlan, S. Vignolini, *Adv. Mater.* **2020**, *32*, 1906889.
[25] C. Honorato-Rios, J. P. Lagerwall, *Commun. Mater.* **2020**, *1*, 1.
[26] B. Droguet, H. Liang, B. Frka-Petesic, R. Parker, M. De Volder, J. Baumberg, S. Vignolini, *Nat. Mater.* **2021**, *21*, 352.
[27] M. Urbanski, C. G. Reyes, J. Noh, A. Sharma, Y. Geng, V. S. R. Jampani, J. P. Lagerwall, *J. Phys.: Condens. Matter* **2017**, *29*, 133003.
[28] H. Agha, Y. Geng, X. Ma, D. I. Avsar, R. Kizhakidathazhatha, Y.-S. Zhang, A. Tourani, H. Bavle, J.-L. Sanchez-Lopez, H. Voos, M. Schwartz, J. P. Lagerwall, *Light: Sci. Appl.* **2022**, *11*, 309.
[29] M. Schwartz, G. Lenzini, Y. Geng, P. Rønne, P. Ryan, J. Lagerwall, *Adv. Mater.* **2018**, *30*, 1707382.
[30] J. Noh, H.-L. Liang, I. Drevensek-Olenik, J. P. Lagerwall, *J. Mater. Chem. C* **2014**, *2*, 806.
[31] Y. Geng, J. Noh, I. Drevensek-Olenik, R. Rupp, G. Lenzini, J. P. F. Lagerwall, *Sci. Rep.* **2016**, *6*, 26840.
[32] Y. Geng, J.-H. Jang, K.-G. Noh, J. Noh, J. P. Lagerwall, S.-Y. Park, *Adv. Opt. Mater.* **2018**, *6*, 1700923.
[33] H. J. Seo, S. S. Lee, J. Noh, J.-W. Ka, J. C. Won, C. Park, S.-H. Kim, Y. H. Kim, *J. Mater. Chem. C* **2017**, *5*, 7567.
[34] T. Yang, D. Yuan, W. Liu, Z. Zhang, K. Wang, Y. You, H. Ye, L. de Haan, Z. Zhang, G. Zhou, *ACS Appl. Mater. Interfaces* **2022**, *14*, 4588.
[35] A. Belmonte, T. Bus, D. Broer, A. Schenning, *ACS Appl. Mater. Interfaces* **2019**, *11*, 14376.
[36] H. Agha, Y.-S. Zhang, Y. Geng, J. P. F. Lagerwall, *Adv. Photonics Res.* **2023**, *4*, 20200363.
[37] Y. Geng, R. Kizhakidathazhath, J. P. F. Lagerwall, *Adv. Funct. Mater.* **2021**, *31*, 2100399.
[38] M. Schwartz, Y. Geng, H. Agha, R. Kizhakidathazhath, D. Liu, G. Lenzini, J. P. F. Lagerwall, *Multifunct. Mater.* **2021**, *4*, 022002.
[39] Y. Uchida, Y. Takanishi, J. Yamamoto, *Adv. Mater.* **2013**, *25*, 3234.
[40] H. Lee, S. Munir, S. Park, *ACS Appl. Mater. Interfaces* **2016**, *8*, 26407.
[41] D. Myung, S. Park, *ACS Appl. Mater. Interfaces* **2019**, *11*, 20350.
[42] F. Jativa, C. Schütz, L. Bergström, X. Zhang, B. Wicklein, *Soft Matter* **2015**, *11*, 5374.
[43] R. M. Parker, B. Frka-Petesic, G. Guidetti, G. Kamita, G. Consani, C. Abell, S. Vignolini, *ACS Nano* **2016**, *10*, 8443.
[44] L. Onsager, *Ann. N. Y. Acad. Sci.* **1949**, *51*, 627.
[45] J. H. Park, J. Noh, C. Schütz, G. Salazar-Alvarez, G. Scalia, L. Bergström, J. Lagerwall, *Chemphyschem* **2014**, *15*, 1477.
[46] C. Honorato-Rios, C. Lehr, C. Schütz, R. Sanctuary, M. A. Osipov, J. Baller, J. P. Lagerwall, *NPG Asia Mater.* **2018**, *10*, 455.
[47] A. S. Utada, E. Lorenceau, D. R. Link, P. D. Kaplan, H. A. Stone, D. Weitz, *Science* **2005**, *308*, 537.
[48] T. Trittel, T. John, K. Tsuji, R. Stannarius, *Phys. Fluids* **2013**, *25*, 052106.
[49] C. Lei, Q. Li, L. Yang, F. Deng, J. Li, Z. Ye, Y. Wang, Z. Zhang, *Soft Matter* **2019**, *15*, 6504.
[50] G. Guan, Z. Zhang, Z. Wang, B. Liu, D. Gao, C. Xie, *Adv. Mater.* **2007**, *19*, 2370.
[51] X. Mu, D. G. Gray, *Cellulose* **2015**, *22*, 1103.
[52] R. M. Parker, T. H. Zhao, B. Frka-Petesic, S. Vignolini, *Nat. Commun.* **2022**, *13*, 1.
[53] J. Wang, C. Mbah, T. Przybilla, B. Apeleo Zubiri, E. Spiecker, M. Engel, N. Vogel, *Nat. Commun.* **2018**, *9*, 5259.
[54] J. Wang, C. Mbah, T. Przybilla, S. Englisch, E. Spiecker, M. Engel, N. Vogel, *ACS Nano* **2019**, *13*, 9005.
[55] C. Kim, K. Jung, J. W. Yu, S. Park, S.-H. Kim, W. B. Lee, H. Hwang, V. N. Manoharan, J. H. Moon, *Chem. Mater.* **2020**, *32*, 9704.
[56] F. Livolant, M. Giraud, Y. Bouligand, *Biol. Cell.* **1978**, *31*, 159.
[57] Y. Bouligand, F. Livolant, *J. Phys.* **1984**, *45*, 1899.